Supramolecular Synthesis of Dithienylethene-Albumin Complexes for Enhanced Photoswitching In Photoacoustic Imaging-Guided Near-Infrared Photothermal Therapy

Xiaoqiong Tan, Yongchao Wang, Hao Li, Yatong Duan, Boxin Wen, Jing Zhao, Heejeong Kim, Jin Yong Lee, Liming Zhou, Hong-Bo Cheng, and Juyoung Yoon**

Photoswitchable molecules can transit between two distinct isomers, enabling them to perform highly controllable imaging and therapeutic functions under certain laser irradiation. Dithienylethenes (DTEs), a class of photoswitchable molecules, exhibit strong thermal stability and high fluorescence quantum yield. However, the short excitation wavelength poses a significant challenge for the application of DTEs in photocontrolled imaging and therapy. Therefore, the development of DTE-based derivatives or hybrid materials with near-infrared (NIR) excitation is of great importance. In this study, two novel DTE derivatives are synthesized, whose closed-ring isomers exhibit strong absorption in the NIR region. Compared with a DTE derivative previously reported and commercially available ones, these two DTE derivatives show higher photoswitching efficiency and extended absorption wavelength. Notably, the supramolecular assembly between DTE derivatives and albumin confers NIR-activated photothermal switching ability on DTE molecules in aqueous solution. In addition, DTE-albumin nanoparticles are further developed to enable photoswitchable photoacoustic imaging (PAI) and photothermal therapy (PTT) for in vivo antitumor applications. Finally, by integrating a thermo-responsive free radical initiator into DTE-albumin nanoparticles, photoswitchable PTT and chemodynamic therapy (CDT) are achieved, effectively inhibiting tumor growth and preventing tumor metastasis.

1. Introduction

Photosensitizers (PSs) are an "all-in-one" tool for disease diagnosis and treatment, owing to their non-invasive properties, high spatiotemporal controllability, and excellent tissue penetration capabilities.[1–3] However, most PSs remain in the "on" state, which unavoidably leads to phototoxicity. Photoswitchable molecules enable the reversible transition between two distinct isomers, which often plays a critical role in modulating their photophysical and chemical properties. This usually brings distinct performance changes in absorption spectrum, fluorescence/phosphorescence emission, electrochemical properties, and so on.[4,5] In the past decades, growing advances have been made in organic photoswitchable molecules for high-resolution imaging, photo-controllable drug delivery, and phototherapy. Among them, P-type Dithienylethene (DTE) with two aromatic groups shows outstanding photoswitching efficiency, fast response rate, robust fatigue

---

X. Tan, H. Li, Y. Duan, B. Wen, J. Zhao, H.-B. Cheng
State Key Laboratory of Organic-Inorganic Composites
Beijing Laboratory of Biomedical Materials
Key Lab of Biomedical Materials of Natural Macromolecules
Beijing University of Chemical Technology
15 North Third Ring Road, Beijing 100029, P. R. China
E-mail: chenghb@mail.buct.edu.cn

X. Tan
Department of Biomedical Engineering
College of Future Technology
Peking University
Beijing 100871, P. R. China

Y. Wang
School of Life Sciences
Zhengzhou University
No.100, Kexuedadao Road, Zhengzhou 450001, P. R. China

H. Li, J. Y. Lee
Department of Chemistry
Sungkyunkwan University
Suwon 16419, South Korea

H. Kim, J. Yoon
Department of Chemistry and Nanoscience
Ewha Womans University
Seoul 03760, South Korea
E-mail: jyoon@ewha.ac.kr

L. Zhou
Henan Provincial Key Laboratory of Surface and Interface Science
Zhengzhou University of Light Industry
Zhengzhou 450002, P. R. China

The ORCID identification number(s) for the author(s) of this article can be found under https://doi.org/10.1002/smll.202409027

[Correction added on March 17, 2025, after first online publication: The copyright line was changed.]

DOI: 10.1002/smll.202409027

resistance and high thermo-stability.[6–8] DTE and its derivatives can undergo reversible isomerization under light irradiation with appropriate wavelength, whose closed-ring state is unable to return to the initial form at room temperature.[4,9,10]

The aggregation of DTE caused by hydrophobicity quenches their photoswitching properties. Rational structure design, group modification, and biomaterial-mediate assembly can address this issue to broaden the application of DTE in photoswitchable biosensing,[11–13] bioimaging[14–17] and photodynamic therapy (PDT).[18–20] For example, two AIE groups were grafted on DTE molecule to achieve photoswitchable PDT and dual-mode photoacoustic imaging (PAI) and fluorescence imaging (FI).[21] Our group has also made some efforts in the DTE-based photoswithchable PDT and bioimaging.[18,19] In a study, the simple supramolecular assembly with albumin restored the photoswitching property of asymmetric DTE molecules in the aqueous phase. The resultant DTE-based nanoparticles successfully achieved control over the “on/off” states by switching between UV and NIR light irradiation, enabling photoswitchable imaging-guided PDT on tumors.[18]

Photothermal agent (PAT)-based PTT possesses good tumor ablation capability, in which the light energy is absorbed by PAT and is converted into heat energy for cell apoptosis as the temperature increases.[22] Despite the strong NIR absorption and high photothermal conversion efficiency, most PATs are unable to govern the initiation and termination of photothermal conversion. Equipping the PAT with responsiveness to endogenous stimuli, such as pH, H_2O_2, and glutathione, can address this issue, but necessitate sufficient stimulation intensity and sensitivity of response.[23–25] By contrast, photoswitchable molecule-based PAT in response to exogenous light provides an alternative for the remote control of photothermal conversion to improve PTT. However, few works have proposed tunable photothermal conversion capacity by photoswitchable molecules.[26,27] Moreover, whether the photothermal conversion property of DTE or other photoswitches can be used for PTT against tumors in vivo is unknown.

Herein, we integrated DTE molecules and thermal initiator, 2,2′-azobis[2-(2-imidazolin-2-yl) propane] dihydrochloride (AIPH) with albumin by supramolecular assembly strategy to achieve synergetic PTT and chemodynamic therapy (CDT) against tumors (**Scheme 1**). Specifically, we first synthesized two novel DTE derivatives with photoswitchable NIR absorption property and photothermal conversion ability. To solve the high hydrophobicity,[8,28] DTE derivatives were assembled with albumin through a facile supramolecular assembly strategy to enhance the photoswitching properties and photoswitchable photothermal conversion effect of DTE derivatives in aqueous solution. This reinforced the feasibility of DTE molecules for their application in cells and in vivo. Finally, a thermo-driven radical initiator, AIPH, was introduced into the nanoparticle. Under light irradiation, AIPH absorbed heat energy from DTE to generate cytotoxic radicals to synergize PTT for the inhibition of tumor growth and metastasis.

2. Results and Discussion

2.1. Photoswitching Properties of Different DTE Molecules

To explore an excellent photoswitch candidate, we first synthesized several DTE derivatives and investigated their photoswitching and absorption properties along with three commercially available DTE molecules (**Figure 1**). The molecule structures of a series of DTE derivatives were shown in Figure 1a, where **1**–**3** are commercially available DTE molecules, while **4**, **5**,[18] **DTE-Me** and **DTE-n-hexyl** are our synthesized molecules. Given the phototoxicity and weak tissue penetration ability, visible (Vis) or near infrared (NIR) light-activated DTEs are more attractive on the biological application. Incorporating conjugated groups on the side chains or introducing the π-conjugation system onto the central ethene bridge of DAEs are common approach to induce a red-shift in absorption spectra.[8,10,29,30] Here, we synthesized four DTE derivatives with cyanoethylene and/or phenylpyridine on the side chains of DTE core that features a π-conjugated skeleton for red-shift of absorption region. The photoswitching behavior of DTE derivatives in dimethyl sulfoxide (DMSO) solution upon irradiation of 365 nm light was observed by UV–vis absorption spectra (Figure 1a–h). After irradiation, the results of our synthesized DTE molecules all occurred a new peak in longer wavelength region compared to the initial state, due to the photoisomerization from open-ring form to closed-ring form (Figure 1e–h). On the contrary, the absorption spectra of **1** and **3** produced a weak peak, and the absorption of **2** remained almost unchanged (Figure 1b–d). In particular, the closed-ring forms of **DTE-Me** and **DTE-n-hexyl** (denoted as **DTE-Me(c)** and **DTE-n-hexyl(c)**) both showed longer new peaks at 733 and 763 nm respectively than **1**–**5** DTE(c) molecules (Figure 1g,h). Moreover, the new absorption peaks of **DTE-Me** and **DTE-n-hexyl** had significant red-shift to NIR region after UV light irradiation (550–950 nm).

The photoswitching ability of these DTE derivatives was further demonstrated by their color changes before and after UV light irradiation (Figure 1i), which showed that only our synthesized DTE molecules had significant color change from colorless to green and was correlated with the UV–vis absorption results. The reversible photoswitching ability was next explored upon 808 nm light irradiation for 20 min, where all closed-ring forms of DTE derivatives returned to open-ring forms with disappearance of new absorption peaks and restored colors. Additionally, only **DTE-Me** and **DTE-n-hexyl** exhibited slowly photoswitching process from closed-ring form to open-ring form, which revealed the long-time thermal relaxation ability of **DTE-Me** and **DTE-n-hexyl** during the NIR light irradiation period (Figure S7, Supporting Information). The reversible photoswitching behaviors of **DTE-Me** and **DTE-n-hexyl** were also investigated by ^{1}H NMR spectroscopy (Figure S8, Supporting Information). Thereby, we selected **DTE-Me** and **DTE-n-hexyl** as the candidates for next supramolecular assembly and photothermal conversion property examination.

J. Yoon
Gradutate Program in Innovative Biomaterials Convergence
Ewha Womans University
Seoul 03760, South Korea

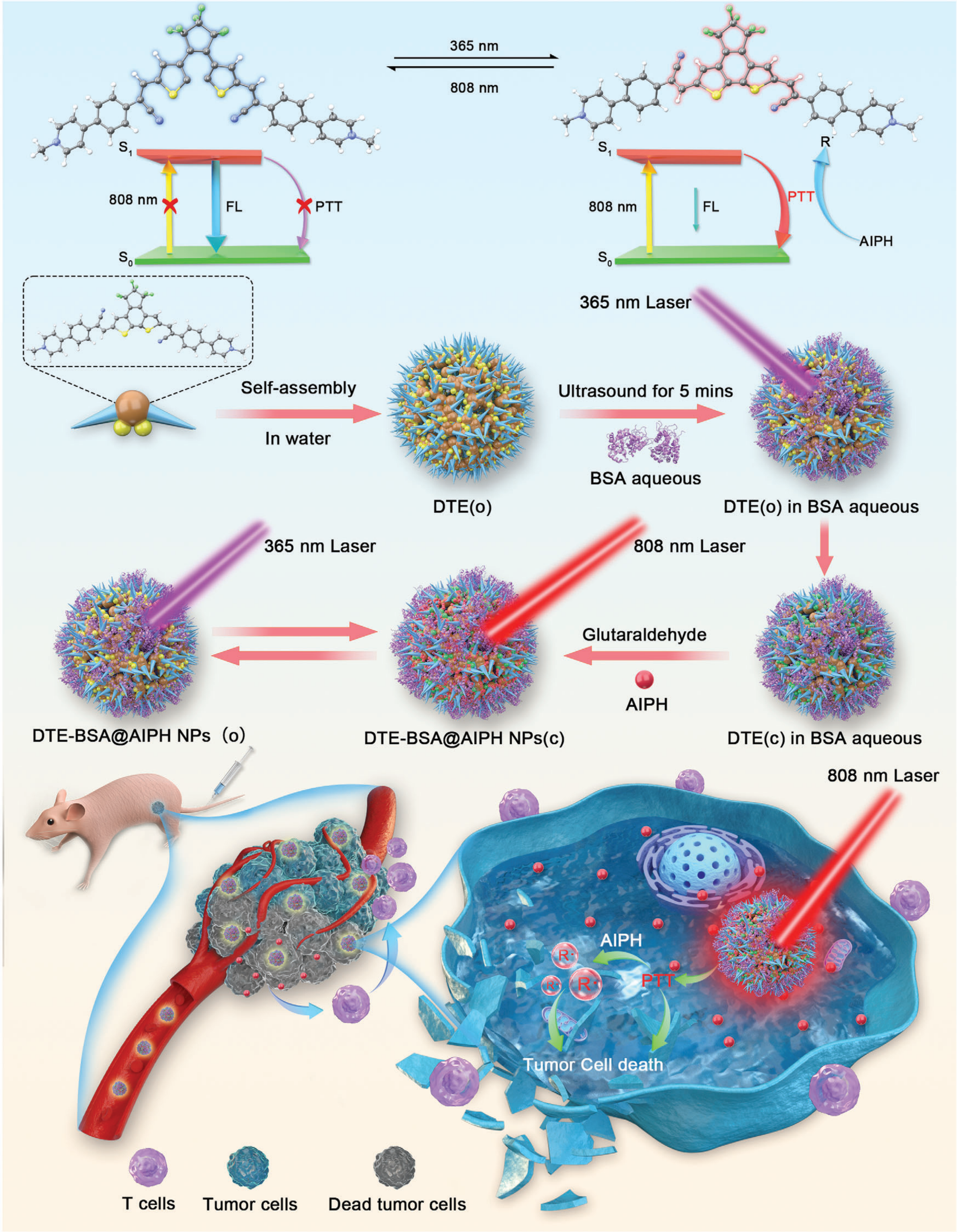

Scheme 1. Schematic illustration of the photoswitching and photothermal conversion processes of NIR DTE molecules and photoswitchable PTT and CDT of DTE-based nanoplatform by a facile supramolecular assembly strategy with AIPH and albumin for antitumor.

2.2. Enhanced Photoswitching and Photothermal Conversion Properties of DTE Molecules by Albumin

Due to the aggregation-caused self-quenching of DTE molecules in aqueous solution greatly hinders its biological application, a facile supramolecular assembly strategy of DTE with albumin has shown improved hydrophilicity and photoswitching property.[12,18] The photoswitching process of DTE with or without albumin in aqueous solution was shown in **Figure** 2a, which demonstrates that DTE molecules in aqueous solution cannot

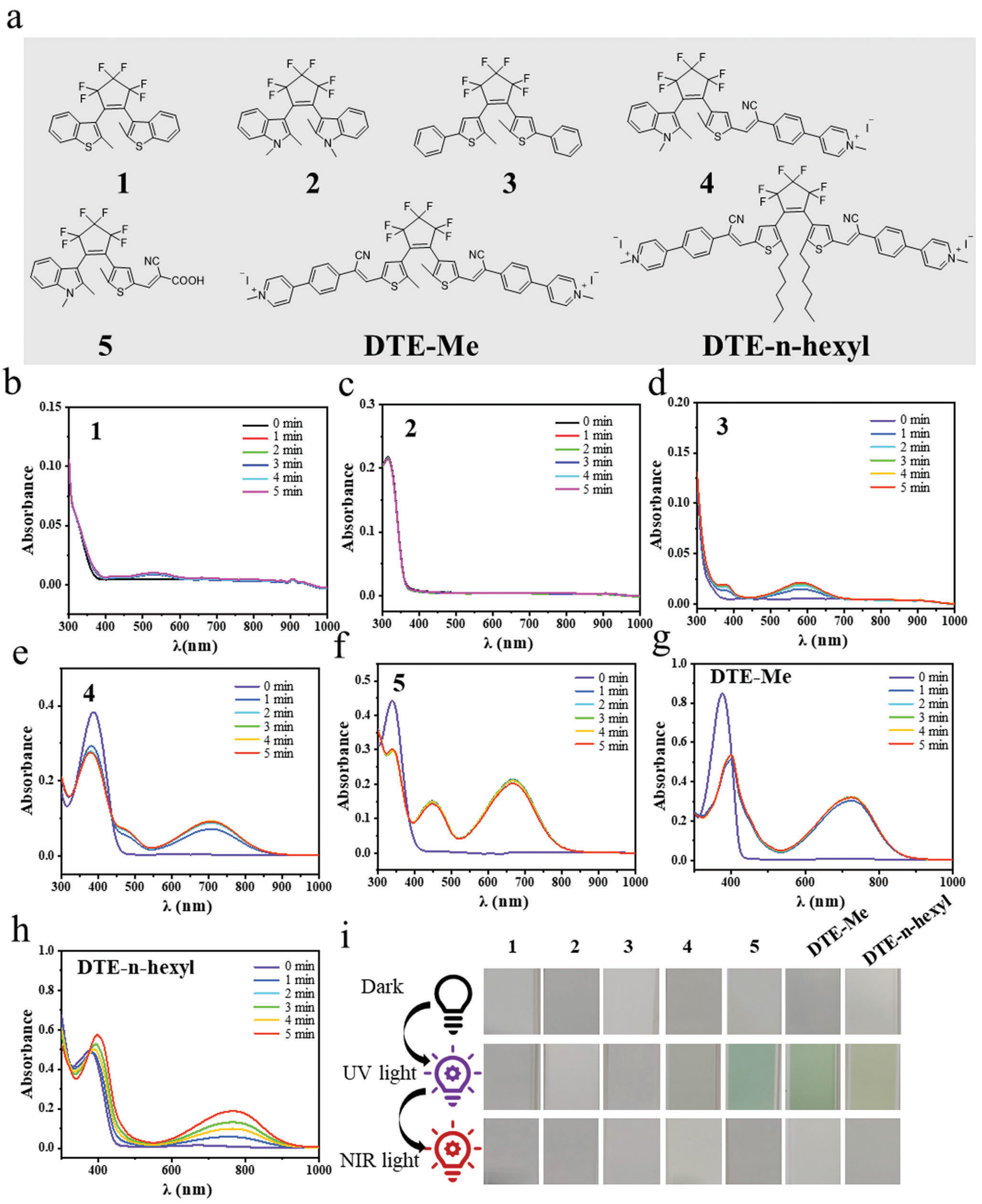

Figure 1. Structure and photoswitching properties of different DTE derivatives. a) Structure list of 7 DTE molecules including **1**, **2**, **3**, **4**, **5**, **DTE-Me,** and **DTE-n-hexyl**. b–h) Absorption spectra of 7 DTE molecules at 20 м in DMSO before and after irradiation of UV light (365 nm) for different time respectively. i) Photographs of 7 DTE molecules before and after irradiation by UV light (365 nm) and then by NIR light (808 nm).

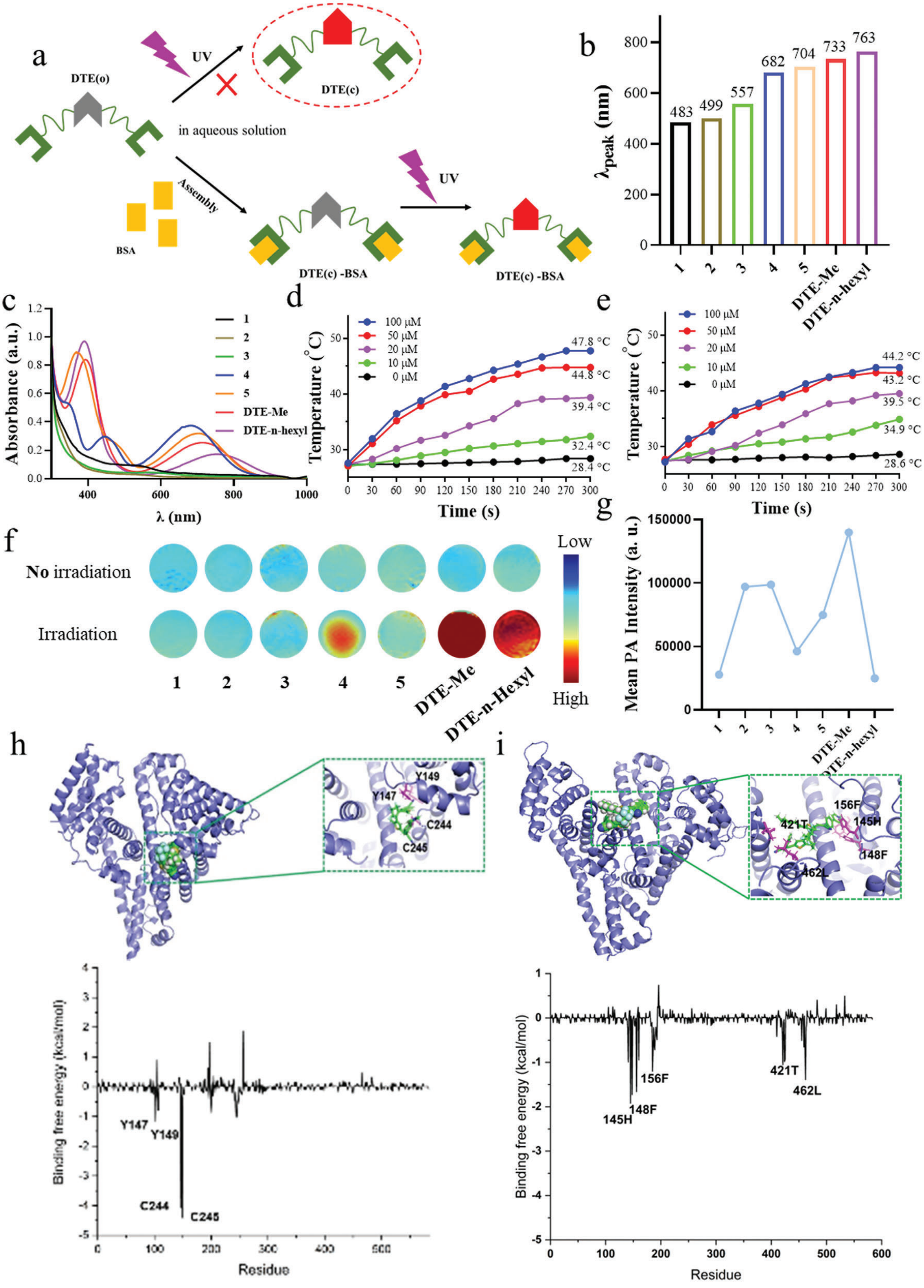
a
DTE(o)
UV
DTE(c)
in aqueous solution
Assembly
BSA
UV
DTE(c) -BSA
DTE(c) -BSA
b
λpeak (nm)
483
499
557
682
704
733
763
1
2
3
4
5
DTE-Me
DTE-n-hexyl
c
Absorbance (a.u.)
λ (nm)
1
2
3
4
5
DTE-Me
DTE-n-hexyl
d
Temperature (°C)
Time (s)
100 μM
50 μM
20 μM
10 μM
0 μM
47.8 °C
44.8 °C
39.4 °C
32.4 °C
28.4 °C
e
Temperature (°C)
Time (s)
100 μM
50 μM
20 μM
10 μM
0 μM
44.2 °C
43.2 °C
39.5 °C
34.9 °C
28.6 °C
f
No irradiation
Irradiation
1
2
3
4
5
DTE-Me
DTE-n-Hexyl
Low
High
g
Mean PA Intensity (a. u.)
1
2
3
4
5
DTE-Me
DTE-n-hexyl
h
Y149
Y147
C244
C245
Binding free energy (kcal/mol)
Residue
Y147
Y149
C244
C245
i
156F
421T
145H
148F
462L
Binding free energy (kcal/mol)
Residue
156F
145H
148F
421T
462L

undergo photoswitching process from open-ring form (DTE(o)) to closed-ring form (DTE(c)) upon UV light irradiation. However, when DTE(o) is co-incubated with bovine serum albumin (BSA), DTE(o)-BSA can be formed by supramolecular assembly. After irradiation of UV light, DTE(o)-BSA can successfully convert to DTE(c)-BSA. Therefore, the supramolecular assembly with BSA can enhance the photoswitching properties of DTE molecules in aqueous solution and is beneficial for the application of DTE molecules in the biological field.

The enhanced photoswitching properties of **DTE-Me** and **DTE-n-hexyl** by BSA were verified with UV–vis absorption spectra. The absorption spectra of **DTE-Me(o)** and **DTE-n-hexyl(o)** in aqueous solution exhibited weak absorption in long-wavelength region (Figure S9, Supporting Information). Interestingly, after co-incubated with BSA in aqueous solution, both the formed **DTE-Me(c)-BSA** and **DTE-n-hexyl(c)-BSA** showed a significant new peak in the range of 500–900 nm, similar to that of **DTE-Me(c)** and **DTE-n-hexyl(c)** in DMSO solution upon UV light irradiation (Figure S10, Supporting Information).

We next investigated the distinction of different DTE derivatives assembled with BSA in aqueous solution upon UV light irradiation by absorption spectra. As shown in Figure 2b, **DTE-Me(c)-BSA** and **DTE-n-hexyl(c)-BSA** held longer absorption peaks in NIR region than other DTE-BSA assemblies (Figure 2c). Therefore, both **DTE-Me(c)-BSA** and **DTE-n-hexyl(c)-BSA** have potential for photothermal conversion since good NIR absorption ability is the key factor in photothermal conversion of PAT.[22]

The photothermal conversion abilities of **DTE-Me-BSA** and **DTE-n-hexyl-BSA** are shown in Figures 2d,e and S11 (Supporting Information). As shown in Figure S11 (Supporting Information), both **DTE-Me(o)-BSA** and **DTE-n-hexyl(o)-BSA** did not show any temperature increase under 808 nm laser irradiation, indicating **DTE-Me** and **DTE-n-hexyl** at open-ring state are unable to convert light to heat energy. On the contrary, the temperatures of **DTE-Me(c)-BSA** and **DTE-n-hexyl(c)-BSA** were increased from room temperature to 47.8 and 44.2 °C respectively and positively correlated with the concentration of DTE molecules. These results suggested that only **DTE-Me(c)** and **DTE-n-hexyl(c)** bound to albumin by supramolecular assembly have the capacity of photothermal conversion.

The photoacoustic imaging (PAI) abilities of different DTE-BSA assemblies were further performed in vitro (Figure 2f,g). The PAI signals demonstrated that only **DTE-Me(c)-BSA** and **DTE-n-hexyl(c)-BSA** possessed excellent photoacoustic properties. This also indicated the better photothermal conversion ability of **DTE-Me(c)-BSA** and **DTE-n-hexyl(c)-BSA** in aqueous solution than other DTE-BSA assemblies due to the correlation between photoacoustic conversion and photothermal conversion. The photoacoustic signal intensity of **DTE-Me(c)-BSA** and **DTE-n-hexyl(c)-BSA** showed a positive correlation with concentration (Figure S12, Supporting Information).

2.3. The Binding Mechanism of DTE-Me and DTE-n-hexyl with BSA

Docking and molecular dynamics (MD) simulations were performed to better understand the binding model between BSA and **DTE-Me(o)** for both antiparallel and parallel open forms. Simulation results suggested two binding sites for the antiparallel form of **DTE-Me(o)**: the FA6 and FA7 (Figure 2h; Figure S13, Supporting Information). However, the parallel form of **DTE-Me(o)** showed two active sites: the cleft and FA5 binding modes (Figures S14 and S15, Supporting Information). As shown in Table S1 (Supporting Information), the binding energy between BSA and the antiparallel form was higher than that with the parallel form. The binding free energy between BSA and **DTE-Me(o)** was calculated to be −41.5 kcal mol^{-1} at the FA7 site, which was much higher than that at the other binding modes for both forms. For this binding mode, four residues (Y147, Y149, C244, and C245) were found to play an important role in the active sites, with decomposed free energies of −4.1, −4.1, −1.0, and −1.0 kcal mol^{-1}, respectively (Figure 2h). The simulation results indicated that BSA is more likely to bind the antiparallel forms of **DTE-Me(o)**, especially at the FA7 region. We also performed docking and MD simulations to investigate the binding model between BSA and **DTE-n-hexyl(o)** for both antiparallel and parallel open forms. Simulations results suggested three same binding modes for antiparallel and parallel open forms of **DTE-n-hexyl(o)**: the FA1 (Heme site), FA7, and cleft region sites (Figure 2i; Figures S16–S20, Supporting Information). In the activate sites (Heme site and cleft region), as shown in Table S2 (Supporting Information), the binding energy between BSA and antiparallel form was much higher than in parallel form. Especially, the antiparallel form of **DTE-n-hexyl(o)** showed the highest binding energy (−43.2 kcal mol^{-1}) with BSA at the cleft region. For this binding mode, five residues (145H, 148F, 156F, 421T, and L462) were found to play an import role in the active sites, with decomposed free energies of −1.9, −1.7, −1.7, −1.1, and −1.4 kcal mol^{-1}, respectively. Two simulations results indicated that the antiparallel forms of **DTE-Me(o)** and **DTE-n-hexyl(o)** are more likely to bind with BSA, especially at activate sites, which is consistent with the supramolecular assembly experiment.

2.4. Construction and Characterization of DTE-Me and DTE-n-hexyl-Based Albumin Nanoparticles

Albumin not only functions as a versatile nano-carrier for drug delivery[31] but also improves the photoswitching properties of DTE molecules.[18] To further evaluate the PTT effect of DTE-BSA assembly in vivo, we constructed albumin nanoparticles by utilizing glutaraldehyde inducing covalent albumin cross-linking for enhancing structural stability and AIPH for synergistic therapeu-

Figure 2. BSA-mediated enhanced photoswitching properties of **DTEs**. a) Scheme of the enhanced photoisomerization of DTE molecule by albumin in aqueous solution from open ring state to closed ring state under UV light irradiation. b) Absorption spectra of 7 DTE molecules in albumin aqueous solution. c) The maximum absorption peaks of (b). d,e) Photothermal curves of **DTE-Me** and **DTE-n-hexyl** at closed-ring form under 808 nm light irradiation at different concentrations in albumin aqueous solution. f) Photoacoustic photographs and g) Mean photoacoustic intensity values of 7 DTE-BSA assemblies in aqueous solution without or with UV light irradiation. h) Binding mode and the free energy of binding of each residue of **DTE-Me** with antiparallel open form at FA7 binding site of BSA. i) Binding mode and the free energy of binding of each residue of **DTE-n-hexyl** with antiparallel open form at cleft region binding site of BSA.

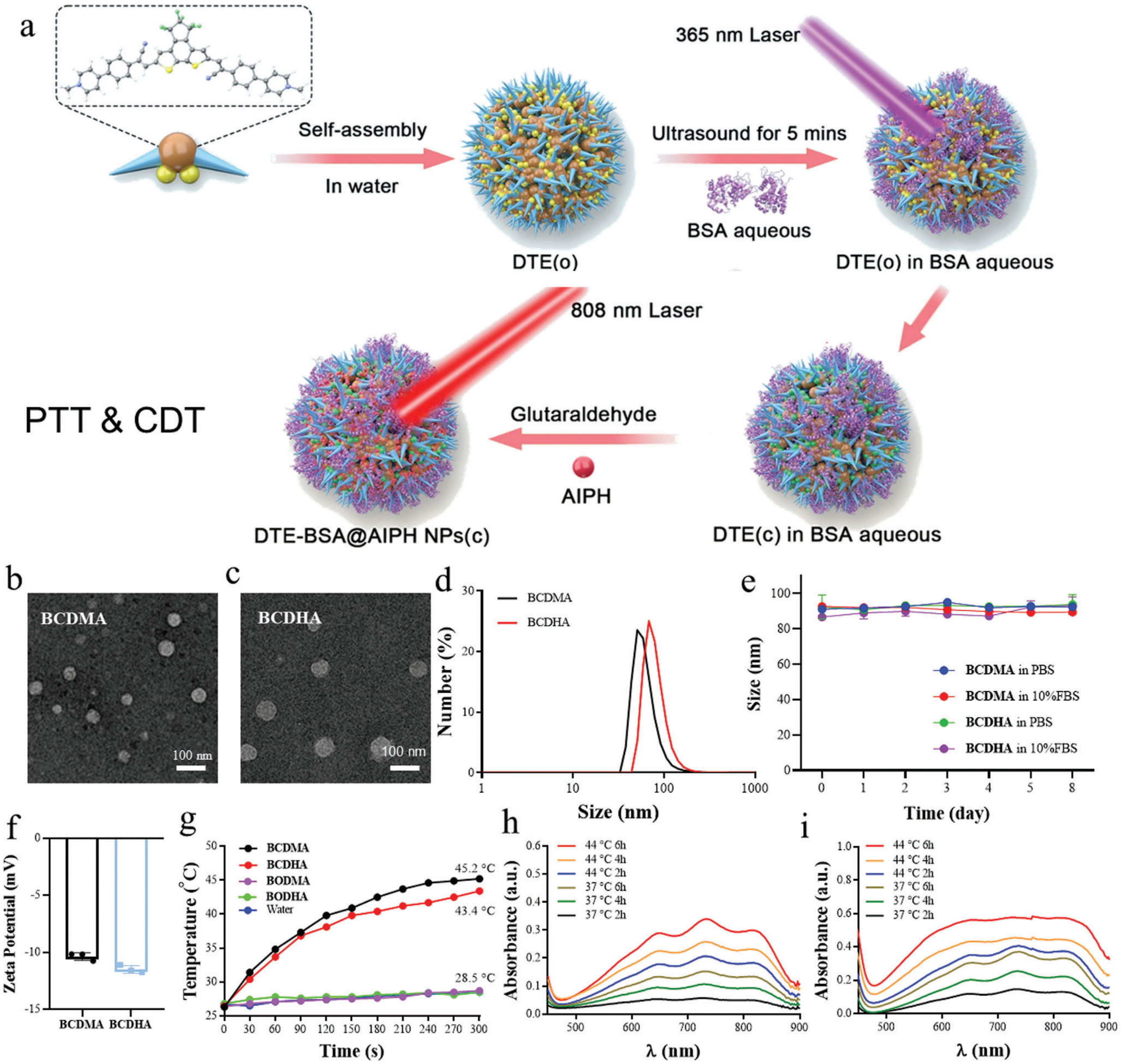

Figure 3. Preparation and characterization of **BCDMA** and **BCDHA** nanoparticles. a) Preparation route of DTE-based albumin nanoparticles. TEM images of b) **BCDMA** and c) **BCDHA**. d) DLS analysis of **BCDMA** and **BCDHA**. e) Hydrodynamic size variation of **BCDMA** and **BCDHA** disperse in 1 × PBS and 10% FBS over 8 days. Data were shown as mean ± s.d. ($n = 3$). f) Zeta potential of **BCDMA** and **BCDHA**. Data were shown as mean ± s.d. ($n = 3$). g) Photothermal curves of **BCDMA**, **BCDHA**, **BODMA**, **BODHA**, and water under irradiation of 808 nm light for 300 s. Generation of ABTS+● as induced by the free radicals released from h) **BCDMA** and i) **BCDHA** at different temperatures and incubation times.

tics with thermodynamic radical generation (**Figure 3a**). At first, DTE molecules (**DTE-Me** or **DTE-n-hexyl**) were co-incubated with BSA in aqueous solution under ultrasound for 5 min to ensure sufficient interaction between DTE with BSA by supramolecular assembly. Then above solution was irradiated by 365 nm light to trigger the photoswitching process of DTE from DTE(o) state to DTE(c) state. Finally, by adding glutaraldehyde into DTE(c)-BSA complex to stabilize the nanoparticles under agitation, the **DTE-Me(c)** or **DTE-n-hexyl(c)**-based albumin nanoparticles, denoted as **BCDM** and **BCDH** were prepared. As above, the albumin nanoparticles constructed with **DTE-Me(o)** and **DTE-n-hexyl(o)** without UV light irradiation were denoted as **BODM** and **BODH**. Finally, the albumin nanoparticles co-encapsulated with **DTE-Me(c)** or **DTE-n-hexyl(c)** with AIPH for combination therapy and were denoted as **BCDMA** or **BCDHA**.

The transmission electron microscopy (TEM) images showed the morphology of **BCDMA** and **BCDHA** were spherical, and the sizes were 50~80 nm (Figure 3b,c). The dynamic light scattering (DLS) measurement demonstrated that the average hydrodynamic diameter of **BCDMA** and **BCDHA** were 66.8 ± 4.3 and

79.8 ± 2.0 nm respectively (Figure 3d). After dispersed in 1 × PBS and 10% FBS over 8 days, the hydrodynamic sizes of **BCDMA** and **BCDHA** were no significant variation, indicating these nanoparticles have high stability (Figure 3e). The zeta potential of **BCDMA** and **BCDHA** were −10.37 ± 0.2 and −11.50 ± 1.2 mV (Figure 3f). Photothermal curves and absorption spectra of different nanoparticles were obtained by an infrared thermographic camera upon 808 nm light irradiation (Figure 3g; Figure S21, Supporting Information). As shown in Figure S20 (Supporting Information), DTE albumin nanoparticles exhibited similar absorption properties with DTE molecules. As shown in Figure 3g, the temperatures of **BCDMA** and **BCDHA** were increased to 42–45 °C (low-temperature photothermal therapy)[32] by irradiation for 5 min, while the temperatures of **BCDMA** and **BCDHA** were the same as that of water without significant increase. The photothermal conversion efficiencies of **BCDMA** and **BCDHA** were calculated to be 14.05% and 14.71%, respectively. (Figure S22a–c, Supporting Information). The thermal conversion results indicated that **DTE-Me(c)** and **DTE-n-hexyl(c)** played key roles in photothermal conversion of nanoparticles which was consistent with **DTE-Me(c)-BSA** and **DTE-n-hexyl(c)-BSA**.

As shown in Figure 3h,i, the generation of ABTS$^{+\bullet}$ exhibited a time-dependent manner when ABTS was incubated with **BCDMA** and **BCDHA** at different temperature, respectively. Whether in **BCDMA** or **BCDHA** group, the absorbance of ABTS$^{+\bullet}$ at 44 °C was obviously higher than that at 37 °C under the same incubation duration, which revealed that AIPH has faster generation rate of free radicals at a relatively higher temperature. Therefore, the integration of DTE-BSA nanoparticles and AIPH for PTT and chemotherapy with free radicals against tumor was a potential and effective synergistic therapeutic strategy.

2.5. Antitumor Effect of BCDMA and BCDHA In Vitro

After confirming the photothermal conversion effect and free-radical generation ability of **BCDMA** and **BCDHA**, we further evaluated the in vitro antitumor efficiency of DTE-based nanoparticles. First, we investigated the cell uptake of **BCDMA** and **BCDHA**. As shown in **Figures** 4a and S23 (Supporting Information), both **BCDMA** and **BCDHA** showed great uptake by 4T1 cells. In addition, increasing the concentration (from 20 to 50 μm) significantly improved cellular uptake of **BCDMA** and **BCDHA**. Further organelle colocalization analysis showed that the majority of both **BCDMA** and **BCDHA** localized in mitochondria while some in lysosomes (Figure S24a–c, Supporting Information). The Pearson correlation coefficients of Cy5-labeld **BCDMA** and **BCDHA** with mitochondria were 0.84 and 0.93, respectively, much higher than that with lysosome (0.27 and 0.23) (Figure S24d,e, Supporting Information) The cytotoxicity of nanoparticles on different cell lines through a cell counting kit-8 (CCK-8) assay. The results showed that more than 90% of the cells (NIH3T3 and HUVEC cells) survived when incubated with **BCDMA** and **BCDHA** at 100 μm for 24 h, indicating good biocompatibility of nanoparticles (Figure S25a,b, Supporting Information). Then, we detected the intracellular free-radical generation using 2′,7′-dichlorodihydrofluorescein diacetate (DCFH-DA) as an indicator. As summarized in Figure 4b,c, in the absence of laser irritation, the cells exhibited negligible fluorescence in all nanoparticles treated groups. However, in the presence of laser irritation, bright green fluorescence was observed in cells incubated with **BCDMA** and **BCDHA**, whereas negligible fluorescence was detected for cells incubated with **BODMA** and **BODHA**. These results validated that a high level of free-radical intracellular was generated by **BCDMA** and **BCDHA**, which was expected to elicit efficient antitumor efficacy.

Subsequently, we examined the cell viability of 4T1 tumor cells after treated with nanoparticles (**BCDM**, **BCDMA**, **BCDH**, and **BCDHA**) upon irradiation. 4T1 cells were incubated with nanoparticles at various concentrations and subjected to irradiation (808 nm, 1.5 W cm^{-2}). As shown in Figure 4d,e, the viability of the cells was relevant to the concentration of the incubated nanoparticles for all the cell groups. For cells treated with **BCDM** and **BCDH**, the cell viability exhibited a mild decrease with more than 60% cells survive at maximum concentration, while the cell viability of cells treated with **BCDMA** and **BCDHA** was drastically decreased to 22.3% at maximum concentration, which is 2.5 times lower than **BCDM** and **BCDH**. These results suggested that the enhanced therapeutic efficacy probably due to the laser-induced synergism between photothermal effect and free radical generation by AIPH.

Moreover, Live/dead staining experiments were performed to further evaluate the therapeutic efficacy of **BCDMA** and **BCDHA**. The live and dead cells were distinguished by dyeing with Calcein AM (green, live cells) and PI (red, dead cells) after various treatment. As shown in Figure 4f,g, strong red fluorescence was detected for cells treated with **BCDMA** and **BCDHA** followed by an 808 nm laser irradiation, indicating that nearly all cells were killed by the treatment. As a comparison, intense green fluorescence was observed in the control groups. To further confirm the therapeutic efficacy, CCK-8 assay, and Live/dead staining experiments were performed on CT26 tumor cells. Consistent with the results of 4T1 tumor cells, incubation of CT26 cells with **BCDMA** and **BCDHA** followed by an 808 nm laser irradiation resulted in significant decrease in the cell viability (Figure S26a–d, Supporting Information). In addition, the apoptosis was assessed by flow cytometric analysis using Annexin V-FITC/ PI apoptosis kit. The results indicated that treatment with **BCDMA** followed by laser irradiation led to significant cell apoptosis, with 32.5% of cell apoptosis which is much higher than the control groups (Figure S27, Supporting Information). Our results confirmed that the photothermal effect by **BCDMA** and **BCDHA** upon laser irradiation was able to induce the generation of intracellular free-radical, successfully driving efficient cell killing by the synergism between PTT and CDT.

2.6. Photoacoustic Imaging and Antitumor Effect of BCDM and BCDMA In Vivo

The biodistribution of **BCDM** and **BCDMA** were investigated by using PAI. 4T1 tumor bearing mice were intravenously injected with **BCDM** and **BCDMA** and the PAI signals were recorded at different time points. As displayed in **Figure** 5a, mice treated with **BCDM** and **BCDMA** exhibited the best enhanced PAI signals at 12 h after injection, indicating that the nanoparticles prominently accumulated at the tumor tissues at this time point.

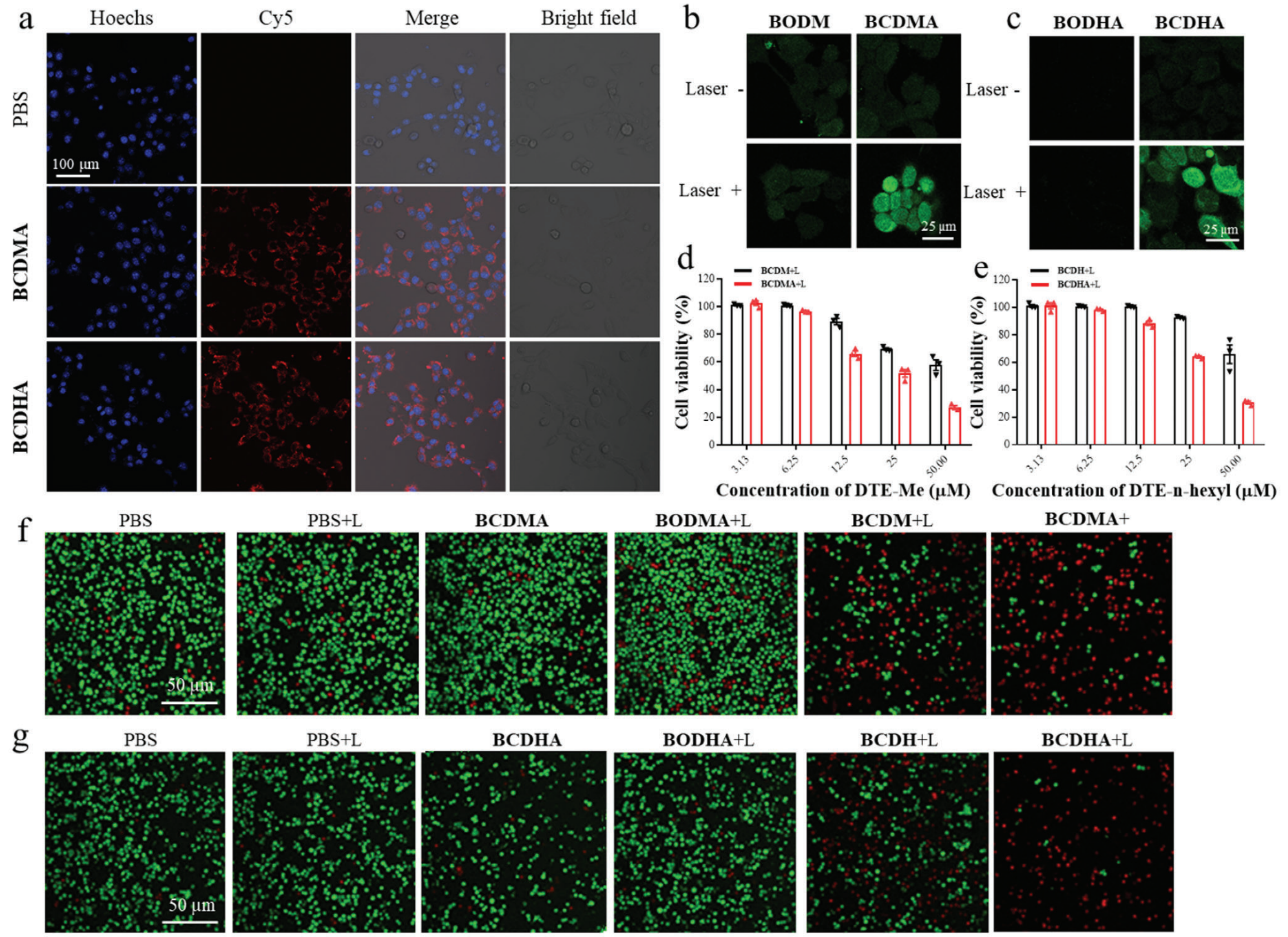

Figure 4. Antitumor effect of **BCDMA** and **BCDHA** in vitro. a) CLSM images of 4T1 cells incubated with cy5-labeld **BCDMA** and **BCDHA** (DTE molecule at a concentration of 50 μM). CLSM observation of free radicals production of 4T1 cells treated with b) **BODMA** or **BCDMA** and c) **BODHA** or **BCDHA** (808 nm, 1.5 W cm^{-2}). Scale bar = 25 μm. Cell viabilities of 4T1 cells incubated with d) **BCDM** or **BCDMA** and (e) **BCDH** or **BCDHA** with NIR light irradiation (808 nm, 1.5 W cm^{-2}, for 10 min). CLSM imaging of 4T1 cells treated with f) **BCDMA** under NIR irradiation (808 nm, 1.5 W cm^{-2}, described as **BCDMA**+L) or control groups (PBS, PBS+L, **BCDMA**, **BODMA**+L and **BCDM**+L) and g) **BCDHA** under NIR irradiation (808 nm, 1.5 W cm^{-2}, described as **BCDHA**+L) or control groups (PBS, PBS+L, **BCDHA**, **BODHA**+L and **BCDH**+L). Calcein-AM (green fluorescence) labeled live cells and PI (red fluorescence) labeled dead cells. Scale bar: 50 μm.

Then we evaluated the antitumor efficacy of **BCDMA** in a breast tumor model. The breast tumor model was established by inoculating 4T1 cells into the left flank of the BALB/c mice as indicated in Figure 5b. The mice were randomly divided into six groups and intravenously treated with different formulations. An NIR laser (1.5 W cm^{-2}, 808 nm) was used to irradiate the tumor site. The treatments were carried out every other day for a total of three times. Body weight and tumor volume were monitored every 3 days. The photothermal curves of tumor site were shown in Figure 5c, demonstrating the significant PTT effect of **BCDM** and **BCDMA**. The results of Figures 5d and S29a (Supporting Information) showed that mice treated with **BCDMA** and **BODMA**+L did not exhibit any significant tumor growth inhibition compared with the PBS control, while mice treated with **BCDM**+L provided moderate tumor growth inhibition. By contrast, **BCDMA**+L induced significant tumor growth suppression. This indicates that the free radicals induced by photothermal effect of **DTE-Me(c)** increased the anticancer activity of **BCDMA**. As shown in Figure S28 (Supporting Information), **BCDMA** did not cause obvious hemolysis after incubation of erythrocytes. In addition, no significant bodyweight loss was observed for all groups during the treatment period (Figure S29b, Supporting Information) which suggests no systemic toxicity was induced by **BCDMA**+L treatment. At the end of study, the mice were euthanized, and the tumors were surgically resected, imaged, weighed and analyzed. The results of Figure 5e,f showed that mice treated with **BCDMA**+L had the smallest tumors with an average tumor mass of 319 mg.

Histopathology analysis of the tumor tissue in each treatment group was performed by H&E staining. As shown in Figure S31 (Supporting Information), mice treated with **BCDMA**+L displayed extensive nuclear shrinkage and fragmentation which indicates that **BCDMA**+L resulted in efficient apoptosis and necrosis of the tumor. Furthermore, histopathology analysis of

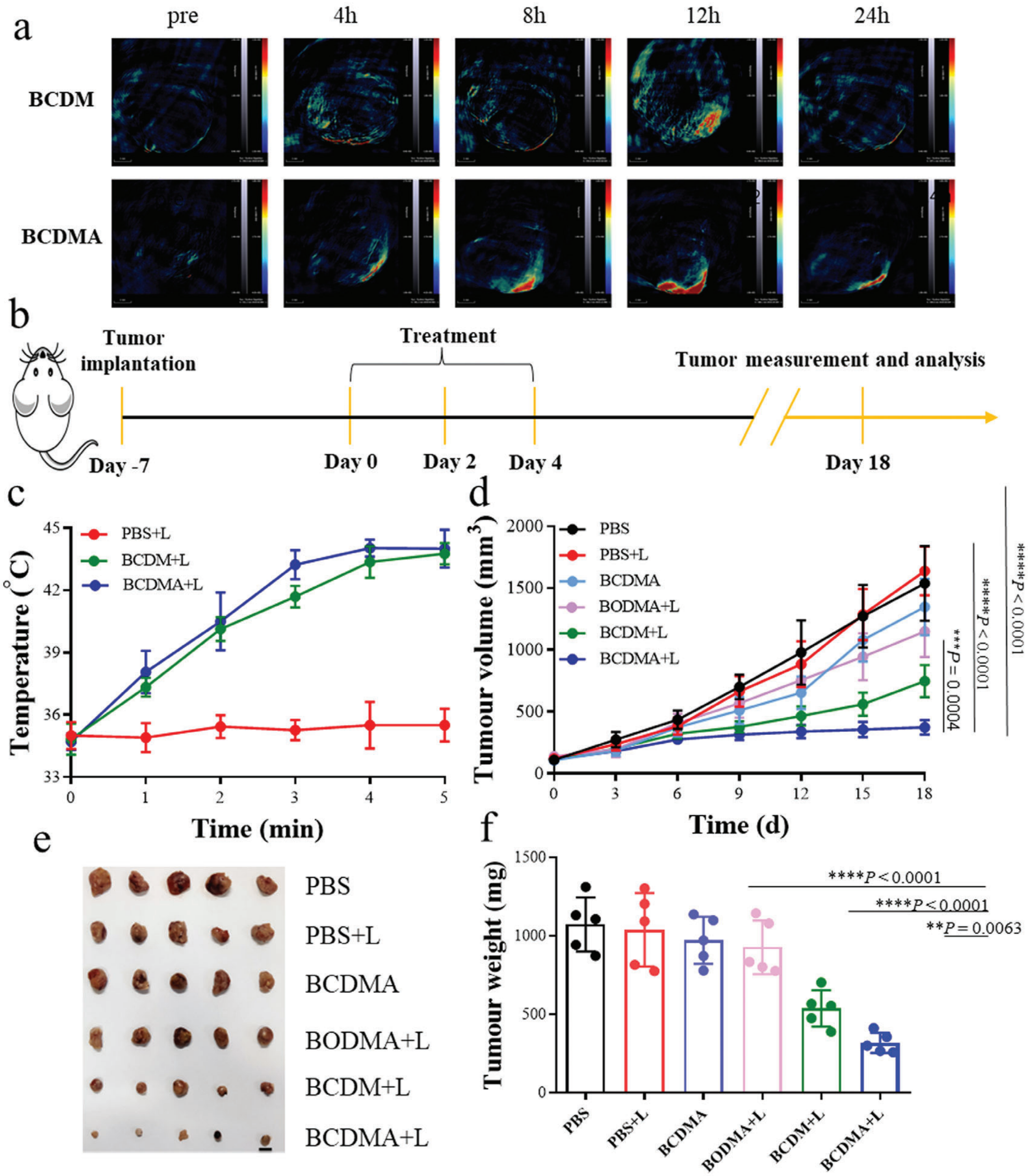

Figure 5. PA imaging and antitumor effect of **BCDM** and **BCDMA** in vivo. a) PA imaging of mice injected with **BCDM** and **BCDMA** at different time points post injection. b) Schematic illustration of experiment to assess the antitumor effect of **BCDMA**. c) Photothermal curves of tumor site after intravenously injection with **BCDM** and **BCDMA** under irradiation for 5 min. d) Tumor volumes of 4T1 were evaluated ($n = 5$). e) Photographs of tumors in the different treatment groups on day 18 (scale bar, 1 cm). f) Average tumor weights of different treatment groups on day 18, $n = 5$.

major organs (heart, liver, spleen, lung, and kidney) revealed that **BCDMA**+L treatment caused negligible histological damage, indicating good biosafety. All these results demonstrated that the supramolecular assembly strategy between DTE(c) and BSA presents outstanding PTT effect and good biosafety, and the combination with thermal free radical initiator further promotes antitumor efficacy. The routine blood test analysis and blood biochemical assay of mice after treated with PBS and BCDMA respectively indicated that BCDMA has a high biosafety (Figures S32 and S33, Supporting Information).

2.7. Antitumor Efficacy of BCDMA on Bilateral Breast Tumor Model

To further confirm the antitumor efficiency of **BCDMA**, we conducted tests on a bilateral breast tumor model. The bilateral breast tumor model was established by sequentially injecting 4T1 cells into the left flank and right flank of the BALB/c mice which were designated as the primary and the abscopal tumors, respectively (**Figure** 6a). The mice were randomly divided into four groups and intravenously injected with different formulations.

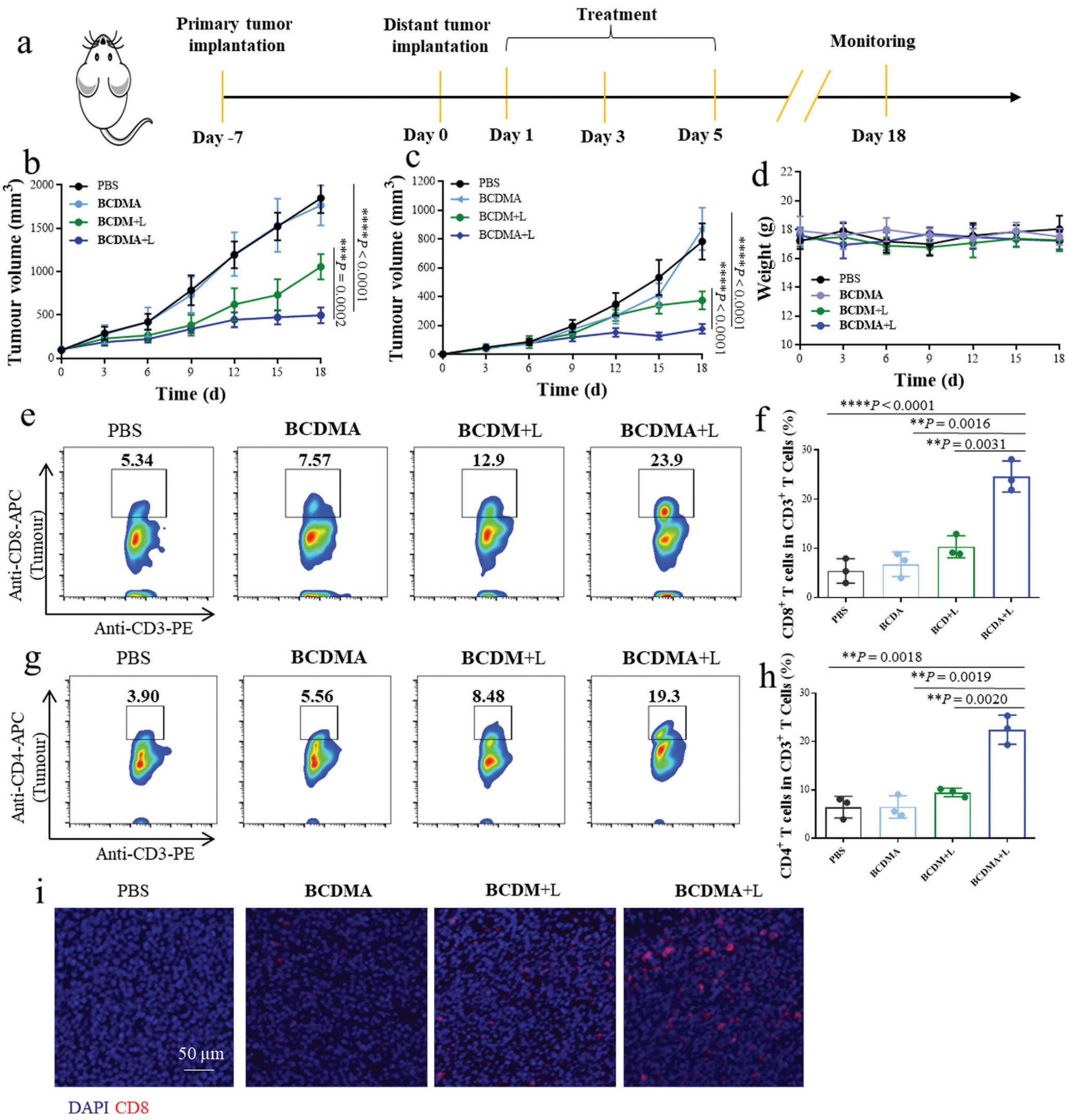

Figure 6. Antitumor effect of **BCDMA** to inhibit primary and distal tumor growth. a) Schematic illustration of experiment to assess the antitumor effect of **BCDMA** to inhibit primary and distal tumor growth. Tumor volumes of the 4T1 b) primary tumors and c) distal tumors from different groups on day 18. d) Mice body weight curves after different treatments. T-cell infiltration was analyzed at day 18 in each group. Flow cytometry analysis and quantification of e,f) $CD8^+$ T or g,h) $CD4^+$ T cells in distal tumors. i) Immunofluorescence staining of $CD8^+$ T cells (red) infiltrated into distal tumors collected on day 18. The data are presented as the mean ± s.d. ($n = 5$) and were analyzed by two-tailed unpaired Student's t-test. NS, no significance; $^{*}P < 0.05$; $^{**}P < 0.01$; $^{***}P < 0.001$; $^{****}P < 0.0001$.

The primary tumors were irradiated with an NIR laser while the abscopal tumors treated without NIR laser. The treatments were performed three times every other day. The antitumor efficacy was evaluated by measuring the primary and abscopal tumor growth. As shown in Figures 6b,c and S30 (Supporting Information), **BCDM**+L could moderately suppress the growth of primary and abscopal tumor, while **BCDMA**+L significantly inhibit the growth of both primary and abscopal tumor. The body weights for the mice in each group showed no significant fluctuation between groups (Figure 6d).

To investigate the mechanism underlying the **BCDMA**+L-induced abscopal tumor growth suppression, we used flow cytometry to evaluate the T cells infiltration in the abscopal tumors (Figure 6e–h). The flow cytometric analysis showed the highest frequency of CD8$^+$ T cells (CD3$^+$CD8$^+$) in the **BCDMA**+L group, which was 4.4-fold higher than that of the PBS group. Consistent with the proportion of CD8$^+$ T cells, the proportion of the CD4$^+$T cells (CD3$^+$CD4$^+$) was dramatically increased to 19.3% which is much higher than the control groups. Moreover, the T cell infiltration was assessed by the immunofluorescence of abscopal tumor. Immunofluorescence analysis of abscopal tumor sections further illustrated that mice treated with **BCDMA**+L showed remarkably increased CD8$^+$ T-cell infiltration compared with the control groups (Figure 6i). These results demonstrated that **BCDMA**+L resulted in improved T-cell infiltration, thus providing effective primary and abscopal tumor growth suppression in vivo.

2.8. The Anti-Metastatic Effect of BCDMA NPs

Finally, we evaluated the efficacy of **BCDMA** in the prevention of tumor metastasis. The tumor metastasis model was established by intravenously injected 4T1 tumor cells into a 4T1 bearing BALB/c mice. Then, the mice were treated with PBS, **BCDMA**, **BCDM**+L, or **BCDMA**+L, respectively (**Figure** 7a). The antimetastatic effect was evaluated by the colonization of tumor cells in the lung. The lungs were surgically removed at the end of the experiment. As indicated by evaluation of lung metastatic nodules, **BCDMA**+L resulted in potent antimetastatic effect which significantly prevent the formation of lung metastases (Figure 7b,c). H&E stain of lung sections showed fewer lung metastases in the **BCDMA**+L group, which further indicates that the lung metastasis was prevented (Figure 7d). The lung weight of mice treated with **BCDMA**+L was lighter than the other treatment groups, probably because of less formation of metastatic nodules (Figure 7e). Moreover, no significant decrease in body weight (Figure 7f) was caused by the treatments. All these results demonstrated that **BCDMA** could induce a significant antitumor immune response to inhibit the lung metastasis of tumor cells.

3. Conclusion

In this work, we have screened 7 similar DTE derivatives and found that two synthetic molecules (**DTE-Me** and **DTE-n-hexyl)** have good photoswitching, NIR absorption and photothermal conversion properties. Further supramolecular assembly strategy with albumin (BSA) enhanced the photoswitching, photothermal and photoacoustic properties of **DTE-Me** and **DTE-n-hexyl** in aqueous solution.

Then **DTE-Me** and **DTE-n-hexyl** were selected as photoswitchable PAT candidates to construct the DTE-based albumin nanoparticles for controllable PTT against tumor. In order to improve the anti-tumor effect, we induced the thermal initiator (AIPH) into DTE-based albumin nanoparticles (**BCDMA** or **BCDHA**) for combination therapy of PTT and CDT. In the in vitro anti-tumor results, **BCDMA** and **BCDHA** showed effective free radical generation and high level of cell death under NIR light irradiation. In vivo photoacoustic imaging showed that DTE-based albumin nanoparticles distributed at tumor site, which indicates their imaging-mediated therapeutic capacity. The in vivo antitumor results revealed that the combination therapy of PTT and CDT is capable of inhibiting tumor growth flowing NIR light irradiation. Furthermore, the combination therapy of **BCDMA** triggered immunotherapy and effectively inhibited abscopal tumor growth and prevented lung metastases.

In summary, we synthesized new DTE molecules by optimization of the skeleton with advanced optical properties. Further supramolecular assembly strategy of DTE-based albumin nanoparticle realized a imaging-mediated triple combination therapy, integrating PTT, CDT, and immunotherapy. More potential applications include photodynamic gene therapy, photocontrolled signaling pathways, and photo-controlled drug release systems of these DTE molecules are expected to be explored.

4. Experimental Section

Materials and Apparatus: 2,2′-azobis[2-(2-imidazolin-2-yl) propane] dihydrochloride were purchased from Macklin, 2,2′-azino-bis(3-ethylbenzothiazoline-6-sulfonic acid) were purchased from Mreda Co., Ltd. Bovine serum albumin, 2′,7′-dichlorofluorescin diacetate, CCK-8 cytotoxicity assay kit and Live/dead cell staining kit were obtained from Solarbio. 0.25% trypsin-EDTA, Hoechst 33 342 and antibiotic solution were obtained from Life Technologies. Cyanine 5 monosuccinimidyl ester was obtained from Solarbio. Antibodies including anti-mouse CD3-PE, anti-mouse CD4-FITC, anti-mouse CD8-APC were purchased from Biolegend. The initial materials are commercially available and have not been further purified.

UV–vis absorption spectra were obtained on a TU-1810 UV spectrophotometer in a quartz cuvette with optical path length 10 mm. Fluorescence emission spectrum were measured in a quartz cuvette on HITACHI F7000 Fluorescence Spectrophotometer. 1H NMR spectra were determined using a Bruker AVANCE III HD 400 spectrometer (400 MHz). High resolution mass (HR-MS) spectra were measured on ESI-TOF MS in MS (+) mode. Dynamic light scattering (DLS) was measured using a Nano-ZS (Malvern). TEM images were recorded on a JEOL-2100F electron microscope operating at 200 kV.

Cell Lines and Animals: 4T1 Cells, CT26 cells, NIH3T3 cells, and HUVECs were purchased from the Institute of Basic Medical Sciences, Chinese Academy of Medical Sciences. 4T1 Cells and CT26 cells were cultured in RPMI-1640 medium containing 10% FBS and 1% penicillin/streptomycin at 37 °C with 5% CO_2. NIH3T3 cells, HUVECs were cultured in DMEM medium containing 10% FBS and 1% penicillin/streptomycin at 37 °C with 5% CO_2. All the cell lines authentication was conducted by a short tandem repeat DNA profiling and confirmed the cells were not contaminated by mycoplasma. BALB/c mice (6–8 weeks old) were purchased from the Experimental Animal Center of Zhengzhou University and maintained in a 12 h light-dark cycle at 25 °C, 40% relative humidity with free access to food and water. All animal experiment protocols were approved by the Institutional Animal Care and Use Committee of Zhengzhou University (Approval No. ZZUIRB 2023-007).

Synthesis of Nanoparticles: **BCDMA** was prepared according to a modified method. Briefly, 39 mg BSA was dissolved in 2 mL deionized water. **DTE-Me** dissolved in DMSO was added dropwise into the above solution (BSA and **DTE-Me** with a molar ratio of 3:1). The mixture was shaded from light and kept sonicating at room temperature for 5 min. Subsequently, the mixture was irradiated with UV light (254 and 365 nm) for 30 min. 100 mg AIPH dissolved in 2 mL deionized water was added to the mixture and kept in the dark for 12 h. Then, 1 mL ethanol and 100 µL 8% glutaraldehyde in ethanol were successively dropped into the mixture via an automatic injection pump. After that, the suspension was purified via centrifugation and washed with water. **BCDHA**, **BODMA**, and **BODHA** were prepared using similar methods (**BODMA** and **BODHA** do not need UV light irradiation).

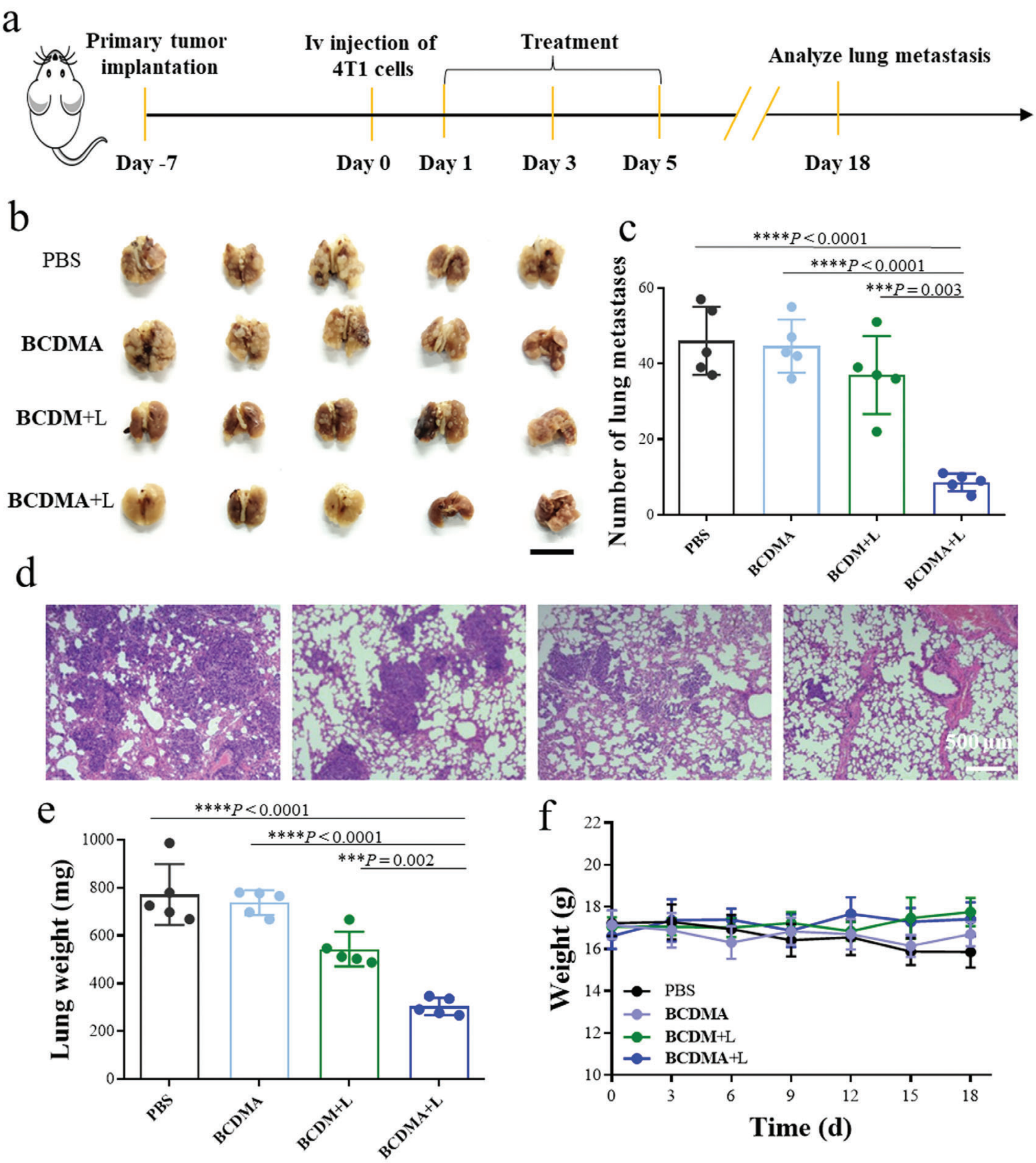

Figure 7. **BCDMA** inhibits the progression of lung metastasis with an improvement in survival. a) The schedule for the model construction and treatment. b) Photographs of lungs harvested on day 18 from mice receiving different treatments (($n = 5$, scale bar: 1 cm)). c) The metastatic nodules were calculated ($n = 5$). d) H&E staining of lungs collected from the treated mice. The black arrows indicated tumor metastases. Scale bar: 1 cm. e) The Weight of the lung tissues were determined. f) The change in body weight of mice during the treatment period. The data are presented as the mean ± s.d. and were analyzed by two-tailed unpaired Student's t-test. NS, no significance; $^{*}P < 0.05$; $^{**}P < 0.01$; $^{***}P < 0.001$; $^{****}P < 0.0001$.

Characterization of Nanoparticles: The hydrodynamic diameter and zeta potential of nanoparticles were characterized using a Zetasizer (Nano ZS, Malvern). The morphology of nanoparticles were characterized using a transmission electron microscope (Ht 7700, Hitachi), respectively. The amount of **DTE-Me**, **DTE-n-hexyl** and AIPH in the nanoparticles was determined by measuring the UV–vis absorbance intensity at 733, 763, and 366 nm, respectively.

Analysis of Photothermal Properties: **BCDMA** and **BCDHA** were dispersed in PBS (100 μm for **DTE-Me** and **DTE-n-hexyl**). Then 1 mL solution was added into a cuvette and irradiated with an 808 nm NIR laser (1.5 W cm^{-2}) for 300 s. The temperature was measured and recorded at 30 s intervals using an infrared imaging device.

Detection of Free Radicals: ABTS was utilized to measure the generation of free radicals of AIPH. The free radicals produced by AIPH are able to oxidize ABTS to generate ABTS+•, which exhibits characteristic absorbance between 500 and 900 nm. **BCDMA** or **BCDHA** solution (AIPH concentration: 1 mg mL^{-1}) and ABTS aqueous solutions with the same concentration was mixed and cultured in dark either in 37 or 44 °C water bath for 2, 4, and 6 h. Then, the absorbance of collected ABTS+• aqueous solution between 400 and 900 nm was measured utilizing a UV–vis spectrometer.

Cellular Uptake: The cellular uptake of **BCDMA** and **BCDHA** was analyzed using confocal laser scanning microscopy (CLSM). Specifically, 4T1 cells were seeded and incubated in 8-well glass bottom plates at 3×10^4

cells per well. Then, the cells were incubated with Cy5-labeled **BCDMA** and **BCDHA** (50 and 20 µm of **DTE-Me** or **DTE-n-hexyl**) for 4 h, and then used for confocal imaging analysis. Cell nuclei were stained by Hoechst for 15 min. After washing with PBS twice, the cells were immediately observed by CLSM.

Free Radicals Generation in Cells: 2′,7′-dichlorofluorescein diacetate (DCFH-DA) was used to detect the generation of intracellular free radicals under light irradiation according to the manufacturer's protocol. Briefly, 4T1 cells were seeded into an 8-well glass bottom plate with a density of 3×10^4 cells per well. The cells were incubated with **BODMA**, **BCDMA**, **BODHA**, and **BCDHA** (50 µm of **DTE-Me** or **DTE-n-hexyl**) and irradiated with or without irradiation (808 nm, 1.5 W cm^{-2} for 10 min).

Live/Dead Staining Assay: The viability of the 4T1 and CT26 tumor cells were assessed using a Calcein-AM/PI Live/Dead cell staining kit, and all experiments were carried out according to the manufacturer's instructions. The 4T1 and CT26 tumor cells were seeded into 6-well plates and incubated overnight. Afterward, the cells were treated with different formulations and irradiated with or without laser irradiation (808 nm, 1.5 W cm^{-2} for 10 min) respectively. After incubation for another 24 h, the cells were collected and stained with AM/PI mixture at 37 °C. Then, PBS was used to wash the cells twice and the fluorescence images of the samples were obtained by the laser scanning confocal microscope (Leica SP8).

In Vivo PA Imaging: 4T1 tumor model was established by subcutaneously injecting 1×10^6 4T1 cells into the left flanks of female BALB/c mice. These mice were divided into two groups randomly when the tumors grew to ≈100 mm^3 in volume. Then these mice were intravenously injected with **BCDM** and **BCDMA** with an equal dose of **DTE-Me** (10 mg kg^{-1}). Next, the mice were placed into a water bath to maintain their body temperature at 37 °C for PA imaging. The real-time PA images were recorded by using a multispectral optoacoutic tomography system (MSOT inVision 128, iThera medical, Germany) at different time points.

Statistical Analysis: Statistical analyses were conducted using GraphPad Prism software (version 8.0) based on data obtained from three or more independent experiments. The data were presented as the mean ± standard deviation (SD). One-way single factorial analysis of variance (ANOVA) was initially performed to evaluate the statistical difference between groups. The statistical difference was expressed as p values: $^{*}p < 0.05$, $^{**}p < 0.01$, $^{***}p < 0.001$, and $^{****}p < 0.0001$.

Supporting Information

Supporting Information is available from the Wiley Online Library or from the author.

Acknowledgements

X.T., Y.W., and H.L. contributed equally to this work. This work was supported by the National Natural Science Foundation of China (22371012), the Natural Science Foundation of Henan (Grant No. 222300420094), the Start-up Grant from Zhengzhou University (Grant No. 32213161), The authors thank Prof. Paul J. Dyson (École Polytechnique Fédérale de Lausanne) for assistance in preparing this manuscript. H. B. Cheng acknowledge the financial support from the China Scholarship Council (CSC) under Grant No. (202306880018). J.Y. thanks the National Research Foundation of Korea (NRF) grant funded by the Korea government (MSIT) (Grant No. 2022R1A2C3005420 and RS-2023-00217701).

Conflict of Interest

The authors declare no conflict of interest.

Data Availability Statement

The data that support the findings of this study are available from the corresponding author upon reasonable request.

Keywords

albumin, dithienylethene, photoacoustic imaging, photoswitching, photothermal conversion

Received: October 2, 2024
Revised: January 17, 2025

---

[1] X. Li, J. F. Lovell, J. Yoon, X. Chen, *Nat. Rev. Clin. Oncol.* **2020**, *17*, 657.
[2] Y.-Y. Zhao, X. Zhang, Y. Xu, Z. Chen, B. Hwang, H. Kim, H. Liu, X. Li, J. Yoon, *Angew. Chem., Int. Ed.* **2024**, *63*, 202411514.
[3] Y.-Y. Zhao, X. Zhang, Z. Chen, Y. Xu, H. Kim, H. Jeong, Y. R. Lee, J. Lee, X. Li, J. Yoon, *Aggregate* **2024**, *5*, e514.
[4] M. Irie, *Chem. Rev.* **2000**, *100*, 1685.
[5] J. Zhang, Q. Zou, H. Tian, *Adv. Mater.* **2012**, *25*, 378.
[6] K. Uno, H. Niikura, M. Morimoto, Y. Ishibashi, H. Miyasaka, M. Irie, *J. Am. Chem. Soc.* **2011**, *133*, 13558.
[7] Z. Zhang, W. Wang, P. Jin, J. Xue, L. Sun, J. Huang, J. Zhang, H. Tian, *Nat. Commun.* **2019**, *571*, E10.
[8] Z. Li, X. Zeng, C. Gao, J. Song, F. He, T. He, H. Guo, J. Yin, *Coord. Chem. Rev.* **2023**, *497*, 215451.
[9] S. Kobatake, S. Takami, H. Muto, T. Ishikawa, M. Irie, *Nature* **2007**, *446*, 778.
[10] S. Lin, K. G. Gutierrez-Cuevas, X. Zhang, J. Guo, Q. Li, *Adv. Funct. Mater.* **2020**, *31*, 2007957.
[11] X. Chai, H. H. Han, Y. Zang, J. Li, X. P. He, J. Zhang, H. Tian, *Beilstein J. Org. Chem.* **2019**, *15*, 2380.
[12] X. Chai, H. H. Han, A. C. Sedgwick, N. Li, Y. Zang, T. D. James, J. Zhang, X. L. Hu, Y. Yu, Y. Li, Y. Wang, J. Li, X. P. He, H. Tian, *J. Am. Chem. Soc.* **2020**, *142*, 18005.
[13] Y. Fu, H. H. Han, J. Zhang, X. P. He, B. L. Feringa, H. Tian, *J. Am. Chem. Soc.* **2018**, *140*, 8671.
[14] D. Kim, A. Aktalay, N. Jensen, K. Uno, M. L. Bossi, V. N. Belov, S. W. Hell, *J. Am. Chem. Soc.* **2022**, *144*, 14235.
[15] C. Wang, Y. H. Liu, Y. Liu, *Small* **2022**, 2201821.
[16] K. Uno, A. Aktalay, M. L. Bossi, M. Irie, V. N. Belov, S. W. Hell, *Proc. Natl. Acad. Sci.* **2021**, *118*, 2100165118.
[17] B. Roubinet, M. L. Bossi, P. Alt, M. Leutenegger, H. Shojaei, S. Schnorrenberg, S. Nizamov, M. Irie, V. N. Belov, S. W. Hell, *Angew. Chem., Int. Ed.* **2016**, *55*, 15429.
[18] H.-B. Cheng, B. Qiao, H. Li, J. Cao, Y. Luo, K. M. Kotraiah Swamy, J. Zhao, Z. Wang, J. Y. Lee, X.-J. Liang, J. Yoon, *J. Am. Chem. Soc.* **2021**, *143*, 2413.
[19] Y. Mi, H. B. Cheng, H. Chu, J. Zhao, M. Yu, Z. Gu, Y. Zhao, L. Li, *Chem. Sci.* **2019**, *10*, 10231.
[20] T. M. Khang, P. Q. Nhien, T. T. K. Cuc, C.-C. Weng, C.-H. Wu, J. I. Wu, B. T. B. Hue, Y.-K. Li, H.-C. Lin, *Small* **2023**, *19*, 2205597.
[21] J. Qi, C. Chen, X. Zhang, X. Hu, S. Ji, R. T. K. Kwok, J. W. Y. Lam, D. Ding, B. Z. Tang, *Nat. Commun.* **2018**, *9*, 1848.
[22] H. S. Jung, P. Verwilst, A. Sharma, J. Shin, J. L. Sessler, J. S. Kim, *Chem. Soc. Rev.* **2018**, *47*, 2280.
[23] G.-l. Wu, F. Liu, N. Li, Q. Fu, C.-k. Wang, S. Yang, H. Xiao, L. Tang, F. Wang, W. Zhou, W. Wang, Q. Kang, Z. Li, N. Lin, Y. Wu, G. Chen, X. Tan, Q. Yang, *Adv. Sci.* **2023**, *10*, 2304104.
[24] K. Zhu, S. Qian, H. Guo, Q. Wang, X. Chu, X. Wang, S. Lu, Y. Peng, Y. Guo, Z. Zhu, T. Qin, B. Liu, Y.-W. Yang, B. Wang, *ACS Nano* **2022**, *16*, 11136.
[25] X. Wei, C. Zhang, S. He, J. Huang, J. Huang, S. S. Liew, Z. Zeng, K. Pu, *Angew. Chem., Int. Ed.* **2022**, *61*, 202202966.

[26] Y. Huang, Y. Pan, X. Zeng, M. Qiu, J. Yin, *Results. Chem.* **2020**, *2*, 100082.

[27] J. Lee, M. M. Sroda, Y. Kwon, S. El-Arid, S. Seshadri, L. F. Gockowski, E. W. Hawkes, M. T. Valentine, J. Read de Alaniz, *ACS Appl. Mater. Interfaces.* **2020**, *12*, 54075.

[28] H. Y. Jung, B. Kim, M. H. Jeon, Y. Kim, *Small* **2022**, *18*, 2103523.

[29] N. M.-W. Wu, M. Ng, W. H. Lam, H.-L. Wong, V. W.-W. Yam, *J. Am. Chem. Soc.* **2017**, *139*, 15142.

[30] C. Li, K. Xiong, Y. Chen, C. Fan, Y. L. Wang, H. Ye, M. Q. Zhu, *ACS Appl. Mater. Interfaces.* **2020**, *12*, 27651.

[31] Q. Chen, Z. Liu, *Adv. Mater.* **2016**, *28*, 10557.

[32] X. Deng, Z. Shao, Y. Zhao, *Adv. Sci.* **2021**, *8*, 2002504.